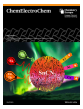

$SnCN_2$: A Carbodiimide with an Innovative Approach for Energy Storage Systems and Phosphors in Modern LED Technology

Cordula Braun,*[a] Liuda Mereacre,[a] Weibo Hua,[a] Tobias Stürzer,[b] Ilia Ponomarev,[c] Peter Kroll,[c] Adam Slabon,[d] Zheng Chen,[e] Yann Damour,[f] Xavier Rocquefelte,[f] Jean-François Halet,[f] and Sylvio Indris[a]

The carbodiimide $SnCN_2$ was prepared at low temperatures (400 °C–550 °C) by using a patented urea precursor route. The crystal structure of $SnCN_2$ was determined from single-crystal data in space group *C2/c* (no. 15) with $a = 9.1547(5)$, $b = 5.0209(3)$, $c = 6.0903(3)$ Å, $\beta = 117.672(3)$, $V = 247.92$ Å^3 and $Z = 4$. As carbodiimide compounds display remarkably high thermal and chemical resistivity, $SnCN_2$ has been doped with Eu and Tb to test it for its application in future phosphor-converted LEDs. This doping of $SnCN_2$ proved that a color tuning of the carbodiimide host with different activator ions and the combination of the latter ones is possible. Additionally, as the search for novel high-performing electrode materials is essential for current battery technologies, this carbodiimide has been investigated concerning its use in lithium-ion batteries. To further elucidate its application possibilities in materials science, several characterization steps and physical measurements (XRD, in situ XANES, Sn Mössbauer spectroscopy, thermal expansion, IR spectroscopy, Mott-Schottky analysis) were carried out. The electronic structure of the *n*-type semiconductor $SnCN_2$ has been probed using X-ray absorption spectroscopy and density functional theory (DFT) computations.

1. Introduction

Cyanamide/carbodiimide compounds with the general formula $M_x(NCN)_y$ (M = alkali, alkaline-earth, transition metals, or metalloids) in which the $(NCN)^{2-}$ ions appear with the carbodiimide ($[N{=}C{=}N]^{2-}$) or cyanamide ($[N{\equiv}C{-}N]^{2-}$) forms, constitute a still rather unexplored family.[1] It is thus essential to elucidate their building mechanisms to better tune their properties and explore their application possibilities in materials science. Carbodiimide and cyanamide $(CN_2)^{2-}$ ions are, due to their divalent anionic charge, frequently considered as pseudo chalcogenides, classified between oxides and sulfides in terms of the Hard and Soft Acids and Bases (HSAB) concept.[2–4] $CaCN_2$,[5–7] commercially known as nitrolime and industrially used as a fertilizer, is the most investigated member of the carbodiimide family. In the last years, many new members have been added due to extensive research following different synthetic routes.[2,3,8–26]

Group 14 nitrides M_3N_4 (M = C, Si, Ge, Sn) are known for their wide-ranging applicability and interesting physical properties.[27–32] Their high-pressure compounds like spinel-type γ-Si_3N_4[33,34] revealed that structures with condensed SiN_6 octahedra result in outstanding micro- and macroscopic materials properties.[30] Concerning the Group 14 carbodiimides having the formula MCN_2, only the Pb compound is known till now.[21] This is quite amazing as advanced non-oxide ceramics in the Si–/C–/N systems are of high technical relevance.

The first crystalline solids in the ternary Si–C–N system, namely silicon dicarbodiimide (SiC_2N_4) and silicon (carbodiimide)nitride (Si_2CN_4) were published by Riedel *et al.*[35] Germanium carbodiimide (Ge_2CN_4) is mentioned in Ref.[36] but no further information is given. Additional investigations on the basis of silylcarbodiimides can be found in Ref.[16].

The first mention of $SnCN_2$ was in a patent[37] being listed among others, although it was at that time still unknown. While $Sn(SCN)_2$[38] has been identified for many years now, just

[a] Dr. C. Braun, L. Mereacre, W. Hua, Dr. S. Indris
Institute for Applied Materials (IAM)
Karlsruhe Institute of Technology (KIT)
Herrmann-von-Helmholtz-Platz 1, 76344 Eggenstein-Leopoldshafen, Germany
E-mail: Cordula.Braun@kit.edu
[b] Dr. T. Stürzer
Bruker AXS GmbH
Oestliche Rheinbrueckenstr. 49, 76187 Karlsruhe, Germany
[c] Dr. I. Ponomarev, Prof. Dr. P. Kroll
Department of Chemistry and Biochemistry
The University of Texas at Arlington
Arlington, Texas 76019-0065, TX, USA
[d] Prof. Dr. A. Slabon
Department of Materials and Environmental Chemistry
Stockholm University
Svante Arrhenius väg 16 C, 106 91 Stockholm, Sweden
[e] Z. Chen
Institute of Inorganic Chemistry
RWTH Aachen University
Landoltweg 1, 52056 Aachen, Germany
[f] Y. Damour, Prof. Dr. X. Rocquefelte, Prof. Dr. J.-F. Halet
Univ. Rennes - CNRS
Institut des Sciences Chimiques de Rennes, UMR 6226
35000 Rennes, France

Supporting information for this article is available on the WWW under https://doi.org/10.1002/celc.202000765

recently new attempts have been made to find $SnCN_2$, which led to $Sn_2O(CN)_2$.[39] Now simultaneously with our patent[40] a new paper of Löber *et al.*[41] just recently appeared indicating the formation of $SnCN_2$ *via* the intermediate compound $Sn_4Cl_2(CN_2)_3$. From the application perspective, there are up to now consequently no reports on the materials properties of $SnCN_2$; especially concerning potential luminescence behavior and energy storage investigations.

Indeed, oxy/cyanamides and carbodiimides constitute a fundamental class of compounds in the field of synthetic solid-state chemistry, which have gained increasing attention within the past decade by revealing remarkably high thermal and chemical resistivities, which makes them excellent candidates for luminescent material hosts, being doped with divalent as well as trivalent rare earth elements.[42–51]

In the domain of batteries, current technologies suffer from a number of challenges and therefore the search for novel high-performing electrode materials is essential. Although there was at first the statement of the carbodiimide $MnCN_2$ to be not electrochemically active in Li-ion batteries,[52] it has been proven in the meantime that transition metal carbodiimides MCN_2 (M = Cu, Zn, Mn, Fe, Co, and Ni) can be applied as negative electrode materials for lithium- and sodium-ion batteries with very good cycling properties.[1,37,53,54]

In this paper, we report an up-and-coming carbodiimide $SnCN_2$ obtained by a novel straightforward synthetic route and its various applications in materials science when doped with suitable cations.

2. Results and Discussion

2.1. Synthesis

The carbodiimide compound $SnCN_2$ was prepared at low temperatures (350–550°) by using an urea precursor route. Doping with the respective metal cations was performed by a subsequent combustion synthesis. For further information see the experimental section and Ref. [40] The crystal structure of $SnCN_2$ was determined from single crystal X-ray diffraction data in space group *C*2/*c* (no. 15) with $a = 9.1547(5)$, $b = 5.0209(3)$, $c = 6.0903(3)$ Å, $\beta = 117.672(3)$, $V = 247.92$ Å^3 and $Z = 4$. The correct unit cell indexing and the structure model were determined from a multi-domain crystal using a BRUKER D8 VENTURE diffractometer with an Incoatec Cu–IμS-Diamond Microfocus Source (4-Circle KAPPA Goniometer PHOTONIII C14, mixed mode Detector).

As the temperature border between the synthesis of $SnCN_2$ and Sn_3N_4 is very small, the synthesis parameters had to be optimized to minimize the Sn_3N_4 amount. Investigations showed that this amount had no influence on the electrochemical results (see battery section). The structure model could be refined based on powder diffraction data as well. (see Figure 1) These were performed on a STOE STADI P powder diffractometer in Debye-Scherrer geometry with Ge(111)-monochromatized Mo-$K\alpha_1$ radiation ($\lambda = 0.709026$ Å) (see Table S1). The sample, not being air sensitive, was enclosed in a glass capillary with 0.3 mm diameter. Our structure model is consistent with the work of Löber *et al.*,[41] except that they have chosen to use the nonstandard setting *I*2/*a* space group to have the monoclinic angle closer to 90°. The observed and calculated X-ray powder diffraction patterns as well as their difference curves after Rietveld refinement[55] are shown in Figure 1. Crystallographic data and details of the Rietveld refinement are listed in Table 1.

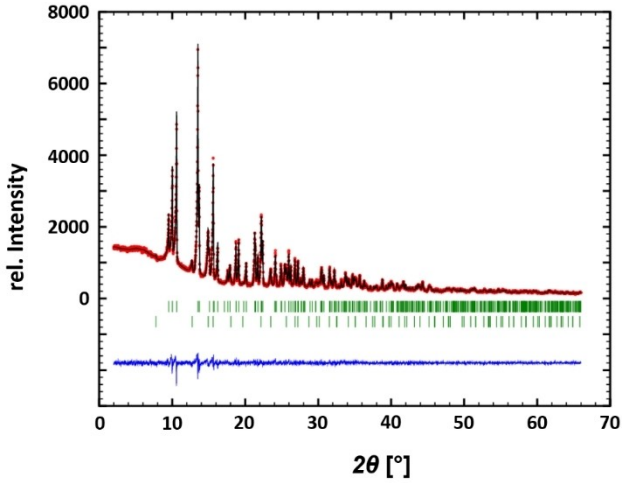

Figure 1. Observed (red circles) and calculated (black line) X-ray powder diffraction pattern of $SnCN_2$ as well as the position of Bragg reflections (green bars) together with their difference curve after Rietveld refinement (λ=0.709026 Å). Bragg reflections: first row represents $SnCN_2$ (88%w/w), second row corresponds to Sn_3N_4 (12%w/w).

For selected bond lengths and angles of $SnCN_2$ and $Sn_2O(CN)_2$[39] see Table 2. A comparison of the lattice parameters of $SnCN_2$ and $Sn_2O(CN)_2$[39] is displayed in Table S1, the occupied Wyckoff sites and refined atomic coordinates of $SnCN_2$ in Table 3 and the anisotropic displacement parameters U_{aniso} are given in Table 4. Finally, EDX measurements of $SnCN_2$ confirmed

Table 1. Crystallographic data for $SnCN_2$, (standard deviation in parentheses).

Formula	$SnCN_2$
Formula mass [g mol^{-1}]	158.71
Crystal system	monoclinic
Space group	*C*2/*c* (no.15)
Cell parameters [Å]	$a = 9.15635(13)$
	$b = 5.01948(7)$
	$c = 6.09086(9)$
	$\beta = 117.65$
Cell volume [Å^3]	247.969(6)
Formula units/cell	4
Diffractometer	STOE STADI P
Radiation [Å]	Mo–Kα_1 ($\lambda = 0.70926$ Å)
Monochromator	Ge 111 (curved)
Temperature [K]	293
Data range (2θ), step width	$2° \leq 2\theta \leq 66°$, 0.01°
Structure refinement	Rietveld refinement, Fullprof[55]
Background treatment	22 fixed background points
Profile function	Pseudo-Voigt (no. 7)
R_{Bragg}	3.35
GoF	1.1
Reduced χ^2	1.19

Table 2. Selected bond lengths [Å] and angles [°] of $SnCN_2$ and $Sn_2O(CN)_2$[39] (standard deviations in parentheses).

$SnCN_2$					
	Atom	Distance		Atom	Angle
1	Sn–N	2.2295(59)	1	N–Sn–N	75
2	Sn–N	2.4779(84)	2	Sn–N–Sn	104
3	C–N	1.2134(76)	3	N–Sn–N	91
4	Sn–Sn	3.7207(5)	4	N–C–N	180
$Sn_2O(CN)_2$					
	Atom	Distance		Atom	Angle
1	Sn–N	2.2148(21)	1	Sn–N–Sn	99
2	Sn–N	2.4403(22)	2	N–Sn–O	78
3	Sn–O	2.0964(13)	3	Sn–O–Sn	106
4	Sn–O	2.3530(15)	4	Sn–O–Sn	111
5	C–N	1.2152(21)	5	Sn–O–Sn	94
6	N–O	2.7223(22)	6	N–C–N	180
	Sn–Sn	3.4683(4)			
	S–Sn	3.5575(3)			

Table 3. Occupied Wyckoff sites, refined atomic coordinates [Å] of $SnCN_2$ (standard deviation in parentheses).

Atom	Wyck.	*x*	*y*	*z*	s.o.f.
Sn	4*e*	1/2	0.28710(13)	1/4	1
N	8*f*	0.6550(8)	0.5962(13)	0.5210(11)	1
C	4*d*	3/4	3/4	1/2	1

the atomic ratio of Sn:N of 1:2 as well as the ratio of C:N of 1:2. No oxygen was detected.

2.2. Description of the Crystal Structure of $SnCN_2$ and Comparison to Other Carbodiimides

The crystal structure of $SnCN_2$, (see Figure 2a) shows along the [010] direction alternating layers of Sn^{2+} atoms and $(N{=}C{=}N)^{2-}$ groups like most of the reported carbodiimides e.g. $Pb(CN)_2$[21] (see Figure 2b). The angle between the Sn atoms and the $(N{=}C{=}N)^{2-}$ groups is much larger (127°) than in $Pb(CN)_2$[21] (116°) and the other carbodiimides, which leads to a much more distorted appearance. The view along the [001] direction reveals that horizontal and vertical zigzag chains of $(N{=}C{=}N)^{2-}$ groups constitute the dominating structure motif being linked *via* two Sn atoms respectively (see Figure 2c). This cross linking leads to a three dimensional network in $SnCN_2$, while in Pb $(CN)_2$[21] separated layers of Pb-$(N{=}C{=}N)^{2-}$ rhombs are found.

Comparing the structures of some Sn-containing carbodiimide family members namely the ones of $SnCN_2$, $Sn_2O(CN)_2$,[39] $Sn(SCN)_2$[38] and $Sn_4Cl_2(CN_2)_3$,[41] it becomes obvious that the structure motifs of $SnCN_2$ and $Sn_2O(CN)_2$[39] are very similar, while $Sn(SCN)_2$[38] and $Sn_4Cl_2(CN_2)_3$[41] display a completely different pattern. (see Figure 3) The crystal structures of $SnCN_2$ and $Sn_2O(CN)_2$[39] are characterized by a three-dimensional network of Sn^{2+} cations and $(N{=}C{=}N)^{2-}$ anionic groups. In $Sn_2O(CN)_2$[39] the oxygen has split up the Sn positions leading to a tetrahedra like Sn_4O formation. (see Figure S1b and Table 2) $SnCN_2$ and $Sn_2O(CN)_2$[39] exhibit two distinct Sn–N distances ($SnCN_2$: 2.229 Å and 2.477 Å, and $Sn_2O(CN)_2$:[39] 2.214 Å and 2.440 Å). For other distances and angles, see the detailed comparison in Figure S1 and Table 2. Finally, both crystal structures of $SnCN_2$ and Sn_2O

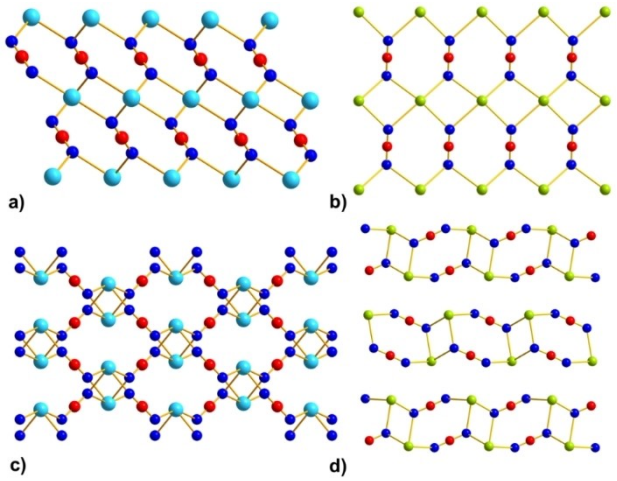

Figure 2. Comparison of a) $SnCN_2$ and b) $Pb(CN)_2$[21] view along [010], c) $SnCN_2$ and d) $Pb(CN)_2$[21] view along [001] direction. (Sn atoms in light blue, C atoms in red, Pb in green and N atoms in blue).

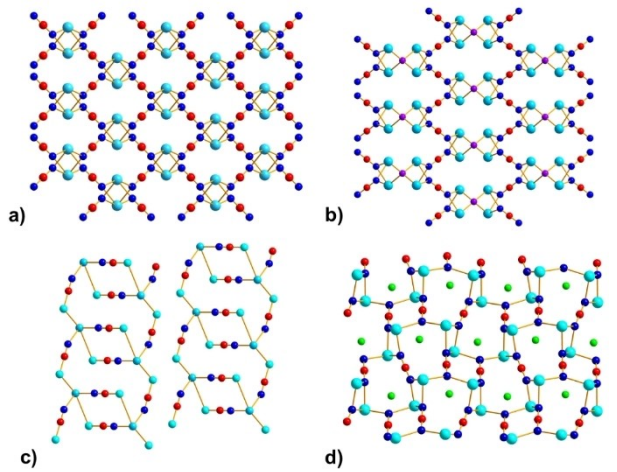

Figure 3. Comparison of a) $SnCN_2$, b) $Sn_2O(CN)_2$[39] view along [001], c) $Sn(SCN)_2$[38] view along [010] and d) $Sn_4Cl_2(CN_2)_3$[41] view along [100]. (Sn atoms in light blue, C atoms in red, Cl in green, N atoms in blue and O atoms in violet .)

Table 4. Anisotropic displacement parameters U_{aniso} [Å^2] of $SnCN_2$ (standard deviations in parentheses).

Atom	U_{11}	U_{22}	U_{33}	U_{12}	U_{13}	U_{23}
Sn	0.0177(6)	0.0122(6)	0.0221(6)	0.00000	0.0072(4)	0.00000
N	0.026(3)	0.018(4)	0.020(3)	−0.004(3)	0.012(3)	−0.001(2)
C	0.007(6)	0.026(5)	0.018(6)	−0.002(4)	0.010(5)	−0.006(4)

$(CN)_2$,[39] contain Sn^{2+} ions sitting at the top of a distorted square pyramid (butterfly-like) "SnN_4" of 2 *mm* symmetry, reminiscent of the isoelectronic hypervalent SF_4 molecule.[56] (see Figure S1c,d) Although $Sn_2O(CN)_2$[39] having completely different lattice parameters (see Table S1) and the structure motif of $Sn_2O(CN)_2$[39] looks much more complex at first sight, the distances and the angles are very similar to those of $SnCN_2$.

The infrared spectrum of $SnCN_2$ shows the nonsymmetric stretch ν_{as} at 1290 cm^{-1}, the symmetric stretch ν_s at 2013 cm^{-1} and the deformation vibrations δ at 664 cm^{-1}, thereby corroborating the symmetric carbodiimide structural motif with two C=N double bonds between carbon and nitrogen (see Figure 4), rendering it isoelectronic to CO_2. These vibrational frequencies match very well with those reported for many known carbodiimides (see Table S2).

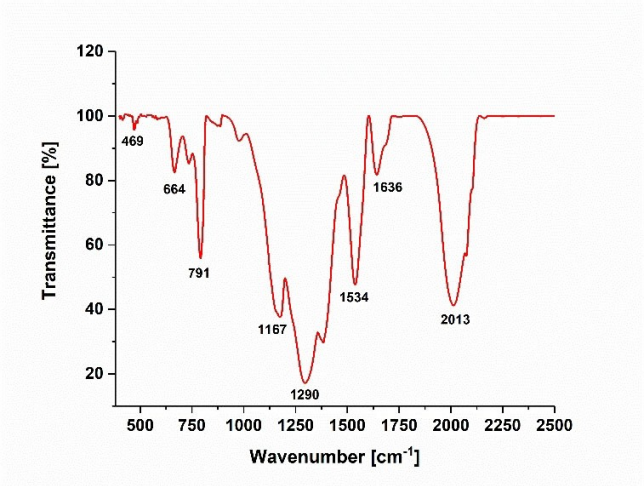

Figure 4. The infrared spectrum of $SnCN_2$.

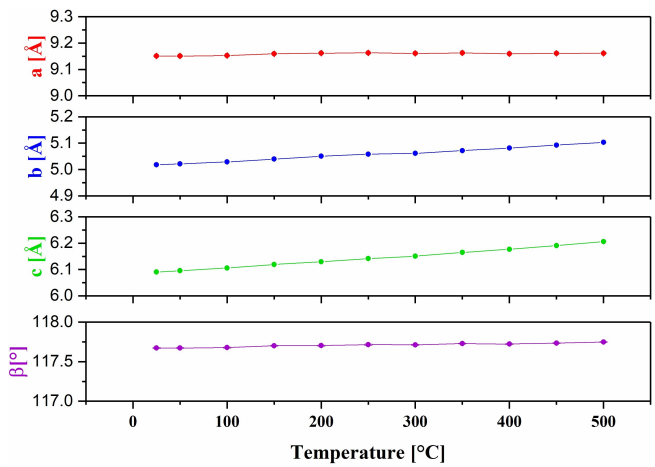

Figure 5. Thermal expansion of $SnCN_2$ in the temperature range between 25 °C and 500 °C, as determined from the Rietveld refinements.

2.3. Thermal Expansion

$SnCN_2$ shows an anisotropic thermal expansion, mainly along the *b*- and *c*-axes. The *a*-axis (0.12 %) shows nearly no expansion with temperature while the *b*- (1.69 %) and *c*-axes (1.88 %) change significantly with temperature. β shows only an extremely small linear temperature dependence (0.02 %). The estimated standard deviations are shown and calculated in agreement with Bérar and Lelann[57] (see Figure 5).

2.4. ^{119}Sn Mössbauer Spectroscopy

Figure 6 shows the Sn Mössbauer spectrum of $SnCN_2$. The spectrum is dominated by a strong doublet with an isomer shift IS = 3.2 mm/s and a quadrupole splitting QS = 1.4 mm/s. The large isomer shift is characteristic of Sn^{2+} with nitrogen neighbors and can thus be assigned to Sn^{2+} in the $SnCN_2$ structure. The slight asymmetry can be ascribed to the vibrational anisotropy of the Sn bonds and/or to texture effects.[58,59] The quadrupole splitting of this doublet reveals an electric field at the site of the Sn nuclei. This gradient is mainly formed by the own electrons of the Sn atoms and, to a lesser extent, by the asymmetry of the neighboring atoms. A second component is visible at IS = 0.3 mm/s with a splitting of QS = 0.6 mm/s. This minor contribution (area fraction of about 15 %) can be attributed to a small amount of Sn^{4+} in this sample. The IS value again hints at nitrogen neighbors. This contribution is thus assigned to Sn_3N_4, in good agreement with the XRD results. (see Table 5)

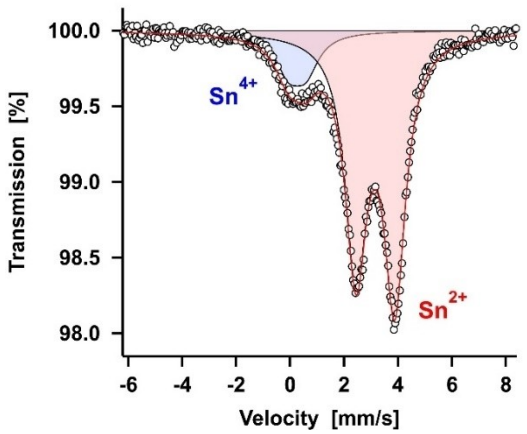

Figure 6. The ^{119}Sn Mössbauer spectrum of $Sn(CN_2)$. Experimental data points are shown as white spheres, the overall fit as a red line, and the sub-spectra are shown as blue and red doublets.

Table 5. Fitting parameters of the contributions used to fit the Mössbauer spectrum of $SnCN_2$. Isomer shift (IS), quadrupole splitting (QS), and line width (Γ) are given in mm/s.

	IS	QS	Γ	Area fraction
Sn^{4+}	0.270 ± 0.019	0.642 ± 0.053	1.156 ± 0.085	14.8 %
Sn^{2+}	3.166 ± 0.003	1.436 ± 0.005	0.973 ± 0.007	85.2 %

2.5. Mott-Schottky (MS) Measurements

The determined electronic band gap from UV- Vis experiments for the brownish carbodiimide powder was 1.6 eV. (see Figure S7) The semiconducting type, valence band edge and conduction band edge positions of $SnCN_2$ and the corresponding doped samples $SnCN_2$:Eu and $SnCN_2$:Eu + Tb were determined by Mott-Schottky (MS) experiments measured at 100 Hz.[60] The three curves exhibit a positive slope, which is characteristic for *n*-type semiconductors (see Figure 7). Extrapolation of the measured data points yields for the undoped $SnCN_2$ a flat-band potential of −0.14 V *vs.* reversible hydrogen electrode (RHE). In combination with the results of the UV-Vis experiments, the conduction band edge and valence band edge values are −0.14 V and 1.41 V *vs.* RHE, respectively. The position of the valence band edge would theoretically make the title compound a potential photo-anode candidate for solar-driven water oxidation. The extrapolation of the MS plots for $SnCN_2$ measured at different frequencies of 10, 100, and 1000 Hz yield almost identical flat-band potentials. Doping $SnCN_2$ with Eu and Tb yields a smaller slope for the curves, i.e., being equivalent to an increase in the charge carrier density, and to a significant shift of the flat band potentials toward smaller values. For $SnCN_2$:Eu and $SnCN_2$:Eu,Tb, the flat-band potentials shift to −0.41 and −0.27 V, respectively. These significant shifts indicate that the dopants are incorporated into the bulk and that doping can be applied to modify the photochemical properties of the pristine $SnCN_2$.[61,62]

2.6. Luminescence Properties

In literature several rare-earth metal doped oxo/carbodiimides or cyanamides are considered to be efficient host candidates for rare-earth activator ions such as Eu^{3+} and Tb^{3+}.[42–51,63,64] Eu^{3+} is considered as an important activator ion with red emission corresponding to the transition of $^5D_0 \rightarrow {}^7F_J$ ($J = 1$–6). The emission of Tb^{3+} is due to the transition between the emitting states of ^5D_J and the excited states of ^7F_J, and the main intense green emission is attributed to the transition of $^5D_4 \rightarrow {}^7F_5$ which is located at approx. 543 nm. But a relevant point here is that the doping ion has been inserted during the main synthesis and not afterwards. In general, doping is performed with Eu^{2+} and only one activator ion is used. Therefore one host shows one colour. In this work, $SnCN_2$ is doped with both, Eu^{3+} and Tb^{3+} activators. Figure 8 shows the CIE 1931 diagram and colours of doped $SnCN_2$, proving that a colour tuning of one host with different activator ions and the combination of the latter ones is possible. This could be demonstrated in the meantime for doped nitrides as well.[32] Additionally, the long-term chemical stability of these carbodiimide phosphors when exposed to air and humidity is provided.

Figure 9a shows that in the emission spectrum of $SnCN_2$ doped with Eu^{3+}, the transitions $^5D_0 \rightarrow {}^7F_0$ and $^7F_3$ seem to be more intense than usually. The $^5D_0 \rightarrow {}^7F_3$ transition is even stronger than the $^5D_0 \rightarrow {}^7F_4$ transition, which is not common. This means a strong *J*-mixing and a strong crystal-field perturbation in this matrix. The $^5D_0 \rightarrow {}^7F_0$ transition is also broad, indicating the location of Eu^{3+} ions in several sites in the host structure (see Figure 9a).

A comparison of the luminescence spectra of $SnCN_2$ and $EuCl_3$ x 6 H_2O is shown in Figure S8. As optical and luminescence spectra are highly sensitive to structural deformation of the nearest environment of rare-earth (RE) ions, it is clearly evident that the spectrum has changed due to the insertion of the Eu cation into the structure of $SnCN_2$. These changes in frequency shift and intensity are in accordance with results of other CN_x:Eu^{3+} compounds in literature.[65,66] A possible avenue to accommodate the total charge neutrality is based on the mixture of the trivalent metal cations (Eu^{3+}, Tb^{3+}) and cation vacancies to balance the total charge and valence. Figure S9 shows a comparison of the X-ray powder diffraction pattern of $SnCN_2$ and $SnCN_2$:Eu.

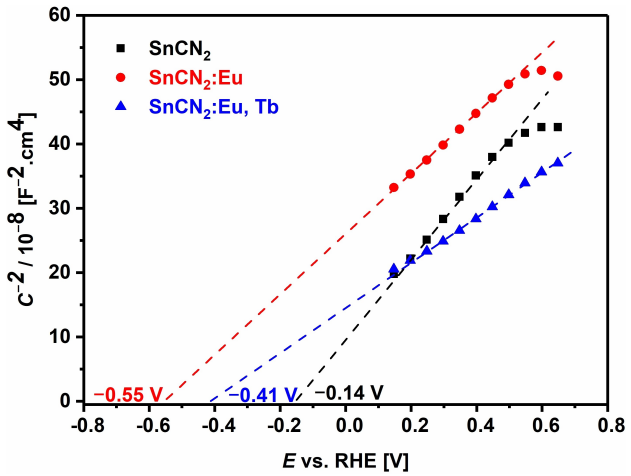

Figure 7. MS analysis of EIS measurements of $SnCN_2$, $SnCN_2$:Eu and $SnCN_2$:Eu,Tb. The intercept corresponds to the extrapolated values for measurements at frequencies of 100 Hz. The concentration of the rare earth elements was 3%.

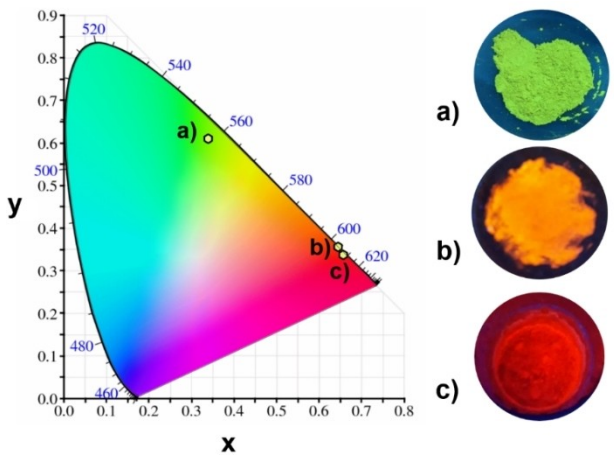

Figure 8. CIE 1931 diagram of $SnCN_2$ doped with a) Tb^{3+}, b) Eu^{3+} and Tb^{3+} and c) Eu^{3+}.

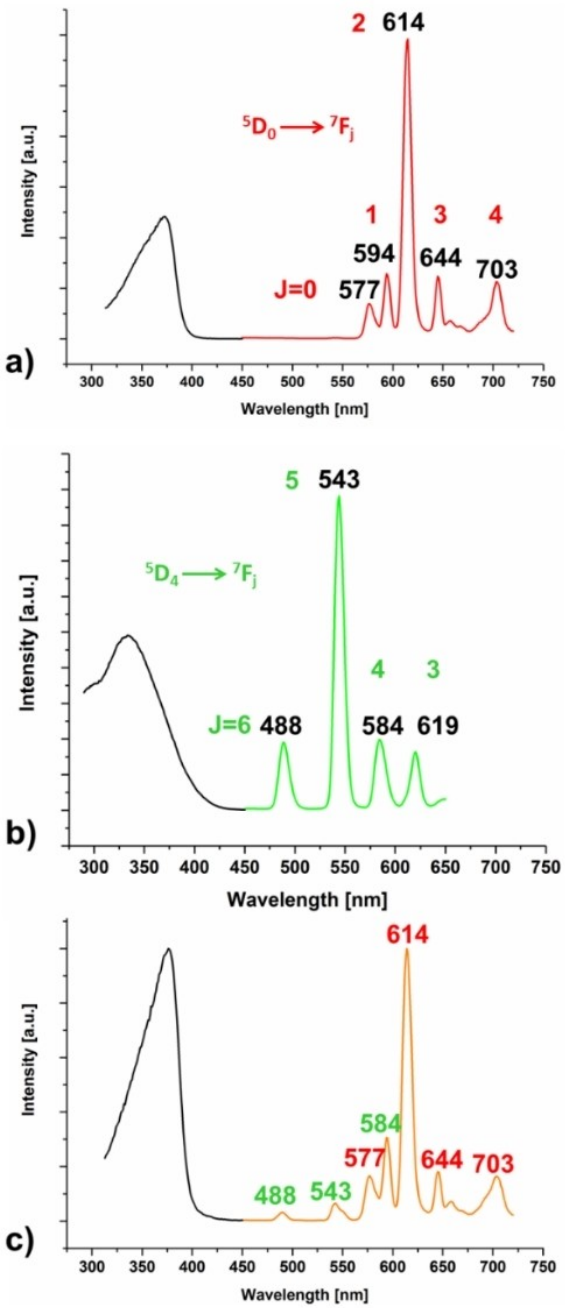

Figure 9. Excitation (black) and emission spectra (colored) of $SnCN_2$ doped with a) Eu^{3+} (red), b) Tb^{3+} (green) and c) Eu^{3+} and Tb^{3+} (orange).

Figure 9b illustrates the excitation (monitored at 543 nm) and emission spectra of Tb^{3+} doped $SnCN_2$. The excitation spectrum exhibits a broad and intense band in the range from 280 nm to 370 nm with a peak at around 334 nm. This broad band is attributed to $4f^8 \rightarrow 4f^7 5d^1$ transitions of the Tb^{3+} ions. The strongest emission peak is at 543 nm corresponding to the $^5D_4 \rightarrow {}^7F_5$ transition, while the peaks at 488 nm, 494 nm, 584 nm and 619 nm, respectively, originate from the $^5D_4 \rightarrow {}^7F_6$, $^5D_4 \rightarrow {}^7F_4$ and $^5D_4 \rightarrow {}^7F_3$ transitions of the Tb^{3+} ions. Figure 9c proves that it is possible to insert two different activator ions in one host showing the typical bands of Eu^{3+} as well as Tb^{3+} in a superposition in one spectrum resulting in an orange colour.

2.7. Battery Investigations

Current battery technologies suffer from a number of challenges, and therefore the search for novel high-performing electrode materials is ongoing.[32] As transition metal carbodiimides MCN_2 (M = Cu, Zn, Mn, Fe, Co and Ni) can be applied as negative electrode materials for lithium- and sodium-ion batteries with very good cycling properties,[1,37,53,54,67] $SnCN_2$ was tested in pure form and doped with several metal cations (M = Ni, Co, Fe, Mn, Zn, Si). (see Figure S2–S4).

The voltage profile observed during galvanostatic cycling of undoped $SnCN_2$ *vs.* $Li^+|Li$ in the voltage range between 3.0 V and 0.01 V is shown in Figure 10a. During the first discharge (see Figure 10a), two regimes are visible in the voltage profile. In the beginning, a first sloping plateau occurs between 1.3 V and 0.5 V with a length of 350 mAh/g, corresponding to conversion of 2.2 Li per formula unit $SnCN_2$. Subsequently, a long second plateau is observed. This plateau has a smaller slope, but still a clear inclination, and its length of 750 mAh/g corresponds to conversion of additional 4.8 Li. During the first charge to 3.0 V, a specific capacity of 300 mAh/g is obtained. This reveals a high irreversible capacity of about 800 mAh/g in the first discharge, and the reversible contribution is only 27% (about two Li per formula unit). During further cycling the two contributions in the discharge voltage profile are still clearly visible, see cycles 2 and 3 in Figure 10a, and the reversible specific capacity stabilizes at 280 mAh/g and for the doped samples between 160–200/280 mAh/g. (see Figure S5, S6) The cyclic voltammogram (see Figure 10b) also reveals two redox processes, in agreement with the galvanostatic measurements. The main contribution is visible at 0.13 V/0.54 V and a second, broader contribution, occurs around 1.0 V. In addition, in the first cycle, another reduction process is visible at 0.65 V, which can be assigned to formation of the solid-electrolyte interphase (SEI). During further cycling, the specific capacity is successively increasing. Such an activation behavior is characteristic of conversion materials with large particle sizes. The strong volume changes during cycling result in fracturing and thus a continuous decrease of the particle sizes and an increased reactivity. The presence of Sn_3N_4, as evidenced by XRD and Mössbauer spectroscopy, might lead to an improved capacity retention as it can act as a buffer to accommodate the strong volume changes during the conversion reaction of $SnCN_2$. Overall, the voltage profile observed during galvanostatic cycling shows some similarity to that observed for SnO[68] that has a structure similar to that of $SnCN_2$,[41] and therefore a similar reaction mechanism can be expected, *vide infra*.

For Ni-doped $SnCN_2$, the galvanostatic cycling and the cyclic voltammogram are shown in Figure 10c and d, respectively. In comparison to the undoped $SnCN_2$ it becomes obvious that additional processes are present, which can be assigned to the redox activity of Ni. In the cyclic voltammogram, two strong processes are visible at 0.63 V/1.45 V and 1.63 V/2.5 V. Further-

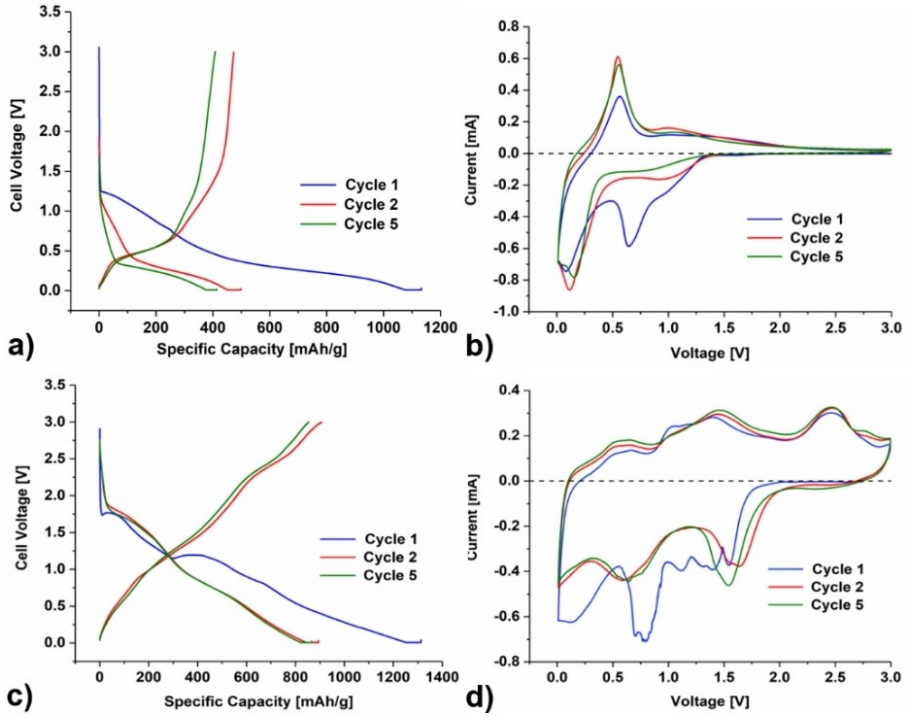

Figure 10. a) Galvanostatic cycling and b) cyclic voltammogram of undoped $SnCN_2$ *vs.* Li^+ | Li c) galvanostatic cycling, and d) cyclic voltammogram of Ni-doped $SnCN_2$ *vs.* Li^+ | Li. All cells were tested with a current density of 100 mA/g in the range of 3.0–0.01 V.

more, the strong oxidation peak at 0.5 V that was present for the undoped sample is strongly suppressed in the Ni-doped sample. This might hint at Ni–Sn alloy formation.[69] Overall, the specific capacity and also the cyclic stability are increased by the doping with Ni. The reversible specific discharge capacity is increased to 800 mAh/g, which corresponds to reversible cycling of 5 Li per formula unit $SnCN_2$.

This doping, improving the capacity enormously, opens up a multitude of degrees of freedom to customize and adapt a battery material to special needs. (see Figure S2–S4) This is even more important as for the search of novel transition metal carbodiimides the right synthetic conditions are often very challenging and now it is possible to overcome this.

Since the sample contains minor impurities of Sn_3N_4, we checked whether this has an influence on the electrochemical behavior. Baggetto *et al.*[70] investigated the electrochemical behaviour of tin nitride and provided valuable information for that. As a first intermediate, Li-Sn-N compounds should become visible upon cycling, decomposing further on into Sn and Li_3N.[70] As we do not see any of these reaction products we can assume a negligible role of the Sn_3N_4 impurity.

2.8. XAS Measurements

Figure 11 shows the *in situ* XANES measurements on the Sn K edge on a battery cell with $SnCN_2$ discharged against a Li metal counter-electrode. During discharging, the absorption spectra (see Figure 11a) do not show a clear shift of the edge position but a change of the shape in the near-edge region and the fine

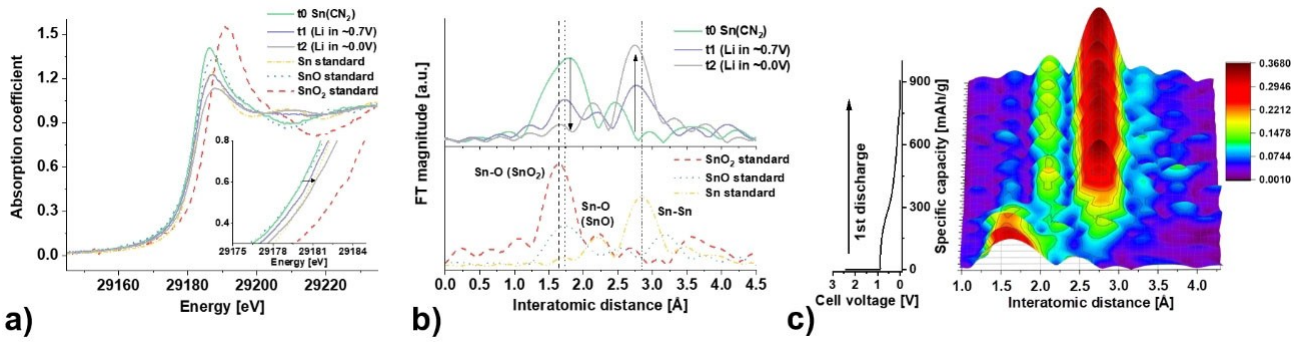

Figure 11. a) Sn K-edge XANES and b, c) k^3-weighted EXAFS spectra of $SnCN_2$-electrode during the first discharge process.

structure. This also becomes apparent in the k^3-weighted Fourier transforms (see Figure 11b and d). In the beginning, a clear peak is visible at 1.8 Å corresponding to the Sn–N bonds being present in the crystal structure of $SnCN_2$. During discharging, this peak successively disappears and a new peak is formed at 2.75 Å. This new peak can be clearly assigned to metallic Sn, as it is confirmed by comparison with the spectrum of the metallic Sn reference foil (see Figure 11b). This spectral evolution shows that the reversible cycling of the batteries is based on the conversion reaction in Reaction (1):

$$Sn(CN_2) + 2\ Li^+ + 2\ e^- \rightleftharpoons Sn^0 + Li_2(CN_2) \quad (1)$$

which is in accordance with the findings of Sougrati *et al.*[1] concerning the electrochemical reaction of transition metal carbodiimides *vs.* $Li^+ \mid Li$.

2.9. Density Functional Theory (DFT) Calculations

DFT calculations were conducted on $SnCN_2$ in order to gain insight into its structural and electronic properties. The structure was first optimized using the VASP program[71–73] at the PBE-ulg[74] and PBE0[75] levels of theory for comparison (see the Appendix for the computational details). Atom cores are described through the projector augmented wave (PAW) method.[76,77] The kinetic energy cutoff for plane wave expansions was set to 500 eV, and the Brillouin zone was sampled by Monkhorst-Pack meshes with a resolution of better than $2\pi \times 1/20$ Å^{-1}.[78] Computed structure parameters are compared to the experimental ones in Table 6. Interestingly, the PBE-ulg and PBE0 approaches differ only slightly, the first somewhat overestimating, the latter somewhat underestimating the experimental metrical parameters. However, both approaches give results in a very good agreement with the experimental data. Indeed, the crystallographic position parameters (one for Sn, three for N) change at most by 0.001, corresponding to a shift of at most 1 pm. Lattice parameters change by less than 1%. Results indicate that the good agreement between computed and experimental data is achieved when adding dispersion interactions to the computations if a GGA functional is used. While the data reported here refer to the universal low-gradient (ulg) method,[74] similar values are computed within the density-dependent energy correction (dDsC) approach.[79] Additionally, the use of a hybrid functional seems to be sufficient to obtain metrical data comparable to the experimental ones.

We tested a variety of different hypothetical structures for $SnCN_2$ at the PBE-ulg level of theory which were derived from suitable and known $M(II)CN_2$ structures: $CuCN_2$,[14] $CdCN_2$,[11] $HgCN_2$,[22] $SrCN_2$,[20] $BaCN_2$,[20] $PbCN_2$.[21][80] In all cases the metal cation was replaced by Sn and the structure was optimized. The experimentally determined structure of $SnCN_2$ was found to be the one with the lowest energy. We note that the $PbCN_2$-type model of $SnCN_2$ (see Figure 2), albeit less favorable, is the only configuration with an enthalpy difference smaller than 10 kJ/mol to the experimentally determined structure of $SnCN_2$. We confirmed that the enthalpy difference between the two different configurations is maintained even through pressures up to 10 GPa.

We complemented our computations by investigating a possible disproportionation of $SnCN_2$ according to Reaction (2):

$$2\ SnNCN \rightarrow Sn + Sn(NCN)_2 \quad (2)$$

We screened a series of structures featuring a metal cation with two polyatomic anions as model compounds of hypothetical $SnCN_2$. Those included $Pb(SCN)_2$,[81] $Hg(SCN)_2$,[82] $Sn(SCN)_2$,[38] $Ba(N_3)_2$,[4] $Cu(N_3)_2$,[83] $Pb(N_3)_2$,[84] $Sr(N_3)_2$,[4] $Hg(N_3)_2$,[85] $Zn(N_3)_2$.[86] With respect to Reaction (2), all these structures are formed with positive reaction enthalpy only. The most favorable structure is that of a $Hg(N_3)_2$-type $SnCN_2$ [2] ($\Delta H > 80$ kJ/mol). While the enthalpy of formation decreases slightly with increasing pressure, we find that at 10 GPa the experimental $SnCN_2$ structure is still stable to disproportionation, with $\Delta H >$ 50 kJ/mol.

Attention is turned next to the bonding analysis of $SnCN_2$. This was nicely done earlier by Meyer and coworkers[41] based on the analysis of its electronic band structure and the electron localization function (ELF).[87,88] This is complemented here by the discussion of the density of states (DOS) and crystal orbital Hamiltonian population (COHP) curves[89] computed with the LOBSTER code.[90–92] The partial and total density of states (PDOS and DOS) of $SnCN_2$ are depicted in Figure 12a. A band gap of approx. 1.5 eV separates the occupied bands from the vacant ones. There is a rather high-energy dispersion, reflecting important covalent interactions not only between C and N

Table 6. Experimental and computed structure data of $SnCN_2$.

	a [Å]	*b* [Å]	*c* [Å]	β [°]	Cell volume [Å^3]	ρ [g/cm^3]	Sn–N [Å]	C–N [Å]
Experiment	9.155	5.021	6.090	117.672	247.92	4.25	2.230 2.478	1.213
Computed (PBE-ulg)	9.205	5.014	6.100	117.22	250.36 (+1.0%)	4.21	2.240 2.465	1.232
Computed (PBE0)	9.045 (−1.2%)	5.067 (+0.9%)	6.047 (−0.47)	117.58 (−0.1%)	245.66 (−0.9%)	4.29	2.216 2.458	1.222
Model	*y* (Sn)	*x* (N)	*y* (N)	*z* (N)				
Experiment	0.28710(13)	0.6550(8)	0.5962(13)	0.5210(11)				
Computed (PBE-ulg)	0.28592	0.65371	0.59522	0.52254				
Computed (PBE0)	0.28803	0.65513	0.59251	0.52149				

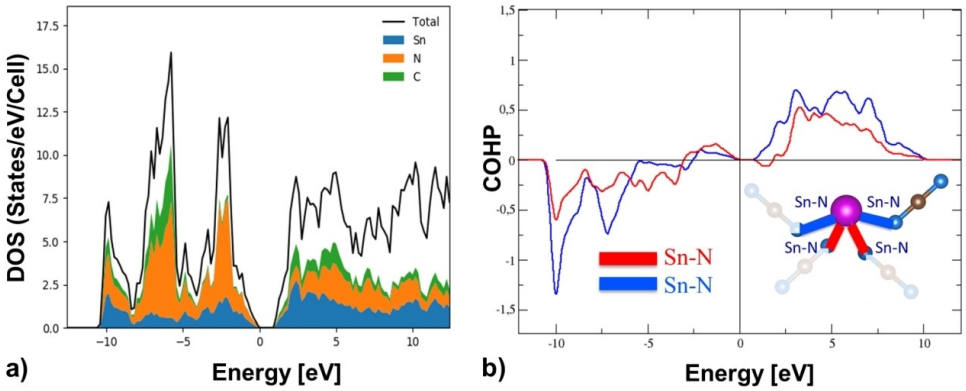

Figure 12. a) Total and atom projected DOS for $SnCN_2$, b) COHP curves for Sn–N contacts in $SnCN_2$.

atoms, but also between the $(CN_2)^{2-}$ anionic units and the Sn^{2+} cations. This is confirmed by the PDOS of the different atoms found dispersed both in the valence and conduction bands. COHP indicating energetic contributions of crystal orbitals between atoms were computed for the two different Sn–N contacts. The resulting curves are sketched in Figure 12b. Their inspection shows that both Sn–N COHP curves show that they are rather similar with the Sn–N bonding states occupied and the antibonding Sn–N states mostly unoccupied. This indicates that the bonding is nearly maximized in this compound. Indeed, we note that close to the Fermi level some weakly antibonding states implying Sn 5s orbital and the N 2p orbitals of the carbodiimide units are present. Integrated COHP (ICOHP) values which are computed for the two different Sn–N contacts, −3.5 and −2.0 Ry per cell, respectively, reflect the different bond strengths of the two Sn–N distances of 2.21 and 2.45 Å, respectively.

3. Conclusions

In this paper, we reported an up-and-coming carbodiimide $SnCN_2$ and its application in materials science when doped with suitable cations. A thorough comparison of its crystal structure with $Sn_2O(CN)_2$ and other related carbodiimides was made. Several characterization steps and physical measurements of the structural and physical properties of the *n*-type semiconductor $SnCN_2$ using various analytical methods (XRD, XAS, Sn Mössbauer spectroscopy, DFT calculations, thermal expansion, IR spectroscopy) were carried out and discussed in detail. Tuning of its materials properties by cation doping led to comprehensive luminescence studies and battery investigations. This confirms the perspectives of $SnCN_2$ as a promising compound for future phosphor converted LEDs and novel high-performing electrode materials for Li-ion batteries with an electrochemical mechanism governed by a conversion reaction. We think that this tuning opens up much more degrees of freedom to customize and adapt a battery material for special needs. Interestingly as well, the luminescence properties of $SnCN_2$ benefit enormously from the fact that it can be doped with several rare-earth metal activator ions, providing different colours.

Experimental Section

Synthesis of $SnCN_2$

$SnCN_2$ was prepared by a low temperature synthesis using a soft urea route. The precursor was obtained by adding tin (IV) chloride pentahydrate ($SnCl_4 \cdot 5\ H_2O$, ≥99%, Sigma Aldrich) powder to ethanol in order to obtain the targeted concentration and form a stable and clear solution. Then urea (≥99%, Sigma Aldrich) was added to the alcoholic solution. This mixture was stirred until the urea was completely dissolved and became a clear solution. The precursor was then put into an oven and treated under a NH_3 atmosphere at 400–550 °C (10 °C/min) for 2 h. Subsequently the sample was cooled down to room temperature in Ar atmosphere.

Doping of $SnCN_2$

The doping of $SnCN_2$ was realised by a successive combustion synthesis.

Therefore the respective metal chlorides (MCl_2 or MCl_3x 6 H_2O), NH_4NO_3, urea and H_2O were added to the sample. This mixture was put into an oven at 600° for 10 min. The doping, which is about 3%, has been checked via EDX measurements.

X-ray Diffraction

Powder Diffraction

X-ray diffraction experiments on powder samples of $SnCN_2$ were performed on a STOE STADI P powder diffractometer in Debye-Scherrer geometry with Ge(111)-monochromatized Mo-$K\alpha_1$ radiation ($\lambda = 0.709026$ Å). The sample was enclosed in a glass capillary with 0.3 mm diameter. A Rietveld refinement has been carried out using the program package Fullprof.[55] Estimated standard deviations are calculated in agreement with Bérar and Lelann.[57]

Single-Crystal Diffraction

Single-crystal X-ray data of $SnCN_2$ were collected on a Bruker D8 VENTURE diffractometer with an Incoatec Cu–IμS-Diamond Microfocus Source (4-Circle KAPPA Goniometer PHOTONIII C14, mixed mode Detector).

EDX Measurements

SEM was performed on a Zeiss Merlin microscope and for EDX we used a Quantax 400 system from Bruker.

^{119}Sn Mössbauer Spectroscopy

^{119}Sn Mössbauer spectroscopic measurements were performed in transmission mode at room temperature using a constant acceleration spectrometer with a $Ca^{119}SnO_3$ source. The velocity scale was calibrated with Sn metal foil and all shifts are given relative to that of $BaSnO_3$.

Infrared Spectroscopy

Infrared spectra were recorded at room temperature using a Bruker Tensor 27 FT-IR spectrometer attached to STA operated under Ar-atmosphere in the range 4000–400 cm^{-1}. To do so, the samples were dispersed in strictly anhydrous KBr and pressed into pellets (Ø 1.3 cm). The spectra were corrected for the presence of KBr.

Mott-Schottky (MS) Measurements

Electrochemical experiments were performed in an electrochemical cell (WAT Venture) in a three-electrode configuration. Platinum and a 1 M AgCl/Ag electrode were used as counter electrode and reference electrode; whereas all recorded potentials were converted *vs.* the reversible hydrogen electrode (RHE) according to $E_{RHE}\ (V) = E_{1M\ Ag/AgCl} + (0.059\ V \times pH)$. Measurements were performed on a BioLogic SP-150 potentiostat operating with the EC Lab Software package. The working electrode was prepared by electrophoretic deposition of $SnCN_2$ on FTO glass.[93]

0.1 M potassium/sodium phosphate (KPi) buffer at pH 7.0 was prepared as the electrolyte with Milli-Q water (18.3 Ω cm) at 298 K. The MS measurements were performed in dark in an electromagnetically shielded box. In the given potential range, a sinusoidal modulation of 10 mV was applied at frequencies of 10, 100, and 1000 Hz with an equilibration time of 10 s.

Luminescence

The luminescence spectra and quantum yield measurements were performed on a Fluorolog®-3 Horiba Jobin Yvon equipped with a TBX detector picosecond photon detection device and a 450 W xenon lamp.

The absolute quantum yields were measured at room temperature in a Horiba Quanta-ϕ F-3029 integrating sphere coupled to the system by a fiber-optic bundle. Data were processed by the FluorEssence™ software (v.3.5.1.20) supplied by Horiba-Jobin-Yvon. The powder samples were prepared by filling the powder into a Spectralon® sample holder covered with a quartz coverslip. As blank a solid body Spectralon® sample was used. The measurements were perfomed as 4-curve method, measuring the Rayleigh lines and luminescence bands in separate datasets for the sample and the blank. The spectra were measured with a step increment of 1 nm and an integration time of 0.1 sec for the Rayleigh lines and 1.0 sec for the emission bands. The excitation and emission slit-widths were set to 1 nm and 2 nm, respectively. Keeping the detector signal in linear range, neutral density filters were applied when necessary. For each sample, excitation and emission spectra were collected to find the corresponding ideal wavelengths.

Battery Investigations

Galvanostatic Cycling

Electrode films were prepared by mixing the active material with SuperP carbon and polyvinylidene fluoride binder in a weight ratio of 70:20:10. A slurry was prepared by addition of N-methylpyrrolidone and then films were cast on Cu foil with a wet thickness of 120 μm and dried at 80 °C for 8 h. Afterwards discs with a diameter of 14 mm were cut from these films and assembled into coin cells (2025 type) with Cellgard 2325 separator, 1 M $LiPF_6$ in ethylene carbonate/dimethyl carbonate (1:1) as electrolyte, and Li metal counter electrode in an argon-filled glove box. Galvanostatic cycling was performed in the voltage range between 3.0 V and 0.01 V with a current density of 35 mA/g. Cyclic voltammetry was done with a sweep rate of 0.1 mV/s in the voltage range between 3.0 V and 0.01 V.

XAS Measurements

X-ray absorption near edge spectroscopy (XANES) was performed on the Sn K edge at the beamline P64 of the PETRA-III synchrotron (DESY, Hamburg). The measurements were done in transmission mode on coin cells with Kapton windows on the front and the back side,[94] a Li metal counter electrode, and 1 M $LiPF_6$ in ethylene carbonate/dimethyl carbonate (1:1) as electrolyte. The C-rate for this experiment was about C/5, i.e. complete discharge within 5 h.

Density Functional Theory (DFT) Calculations

Computational Details

All calculations were carried out within the Density Functional Theory (DFT) as implemented in the Vienna *ab initio* Simulation Package (VASP).[71–73] For electron exchange and correlation we used the Generalized Gradient approximation as parameterized by Perdew, Becke, and Ernzehof (PBE)[95,96] or the hybrid PBE0 functional.[75] Dispersion interactions were treated through the universal low-gradient (ulg) method.[74] Atom cores are described through the projector augmented wave (PAW) method.[76,77] The kinetic energy cutoff for plane wave expansions was set to 500 eV, and the Brillouin zone was sampled by Monkhorst–Pack meshes with a resolution of better than $2\pi \times 1/20$ $Å^{-1}$.[78] Geometries were optimized until forces were converged to lower than 10^{-3} eV/Å and stresses lower than 1 kBar.

DOS and crystal orbital Hamiltonian population (COHP) curves were shifted so that the Fermi level lies at 0 eV. A measure of the magnitude of the bonding was obtained by computing the COHP corresponding to the Hamiltonian population weighted DOS.[89] These curves were projected with LOBSTER[90–92]

Acknowledgement

The authors gratefully acknowledge Udo Geckle (IAM-ESS KIT Karlsruhe) for the EDX, Dr. M. Susana D. Darma (IAM-ESS KIT

Karlsruhe) for high-temperature XRD measurements and Sabine Schlabach (INT KIT Karlsruhe) for luminescence measurements. Furthermore, the financial support by NSF through awards OISE-1743701 and CMMI 1634448 is acknowledged. This work contributes to the research performed at CELEST (Center for Electrochemical Energy Storage Ulm-Karlsruhe). Open access funding enabled and organized by Projekt DEAL.

Conflict of Interest

The authors declare no conflict of interest.

Keywords: carbodiimides · energy storage · lithium · luminescence · tin

[1] M. T. Sougrati, A. Darwiche, X. Liu, A. Mahmoud, R. P. Hermann, S. Jouen, L. Monconduit, R. Dronskowski, L. Stievano, *Angew. Chem. Int. Ed.* **2016**, *55*, 5090–5095; *Angew. Chem.* **2016**, *128*, 5174–5179; *Angew. Chem.* **2016**, *128*, 5174–5179.
[2] X. Liu, M. Krott, P. Müller, C. Hu, H. Lueken, R. Dronskowski, *Inorg. Chem.* **2005**, *44*, 449, 3001–3003.
[3] X. Liu, L. Stork, M. Speldrich, H. Lueken, R. Dronskowski, *Chem. Eur. J.* **2009**, *15*, 1558–1561.
[4] O. Reckeweg, A. Simon, *Z. Naturforsch. B* **2003**, *58*, 1097–1104.
[5] H. Franck, H. Heimann, *Z. Elektrochem. Angew. Phys. Chem.* **1927**, *33*, 469–475.
[6] M. A. Bredig, *J. Am. Chem. Soc.* **1942**, *64*, 1730–1731.
[7] N.-G. Vannerberg, G. Claeson, L. Schotte, A. Block-Bolten, J. M. Toguri, H. Flood, *Acta Chem. Scand.* **1962**, *16*, 2263–2266.
[8] M. Becker, J. Nuss, M. Jansen, *Solid State Sci.* **2000**, *2*, 711–715.
[9] X. Tang, H. Xiang, X. Liu, M. Speldrich, R. Dronskowski, *Angew. Chem.* **2010**, *122*, 4846–4850.
[10] X. Tang, H. Xiang, X. Liu, M. Speldrich, R. Dronskowski, *Angew. Chem. Int. Ed.* **2010**, *49*, 4738–4742.
[11] G. Baldinozzi, B. Malinowska, M. Rakib, G. Durand, *J. Mater. Chem.* **2002**, *12*, 268–272.
[12] M. Launay, R. Dronskowski, *Z. Naturforsch. B* **2005**, 60b, 437–448.
[13] T. D. Boyko, R. J. Green, R. Dronskowski, A. Moewes, *J. Phys. Chem. C* **2013**, *117*, 12754–12761.
[14] X. Liu, M. A. Wankeu, H. Lueken, R. Dronskowski, *Z. Naturforsch. B* **2005**, 60b, 593–596.
[15] X. Liu, R. Dronskowski, R. Glaum, A. L. Tchougréeff, *Z. Anorg. Allg. Chem.* **2010**, *636*, 343–348.
[16] K. Krupinski, Molekulare Silylcarbodiimide-Synthese, Struktur Und Reaktivität, Technische Universität Bergakademie Freiberg, **2012**.
[17] X. Liu, R. Dronskowski, R. K. Kremer, M. Ahrens, C. Lee, M.-H. Whangbo, *J. Phys. Chem. C* **2008**, *112*, 11013–11017.
[18] M. G. Down, M. J. Haley, P. Hubberstey, R. J. Pulham, A. E. Thunder, *J. Chem. Soc. Chem. Commun.* **1978**, *2*, 52–53.
[19] A. J. Corkett, Z. Chen, D. Bogdanovski, A. Slabon, R. Dronskowski, *Inorg. Chem.* **2019**, *58*, 6467–6473.
[20] U. Berger, W. Schnick, *J. Alloys Compd.* **1994**, *206*, 179–184.
[21] X. Liu, A. Decker, D. Schmitz, R. Dronskowski, *Z. Anorg. Allg. Chem.* **2000**, *626*, 103–105.
[22] X. Liu, P. Müller, P. Kroll, R. Dronskowski, *Inorg. Chem.* **2002**, *41*, 4259–4265.
[23] M. Becker, J. Nuss, M. Jansen, *Z. Naturforsch. B* **2000**, *55*, 383–385.
[24] M. Becker, M. Jansen, *Z. Anorg. Allg. Chem.* **2000**, *626*, 1639–1641.
[25] M. Becker, M. Jansen, *Acta Crystallogr. Sect. C* **2001**, 57, 347–348.
[26] L. Stork, X. Liu, B. P. T. Fokwa, R. Dronskowski, *Z. Anorg. Allg. Chem.* **2007**, *633*, 1339–1342.
[27] E. Horvath-Bordon, R. Riedel, A. Zerr, P. F. McMillan, G. Auffermann, Y. Prots, W. Bronger, R. Kniep, P. Kroll, *Chem. Soc. Rev.* **2006**, *35*, 987–1014.
[28] N. Scotti, W. Kockelmann, J. Senker, S. Traßel, H. Jacobs, *Z. Anorg. Allg. Chem.* **1999**, 1435–1439.
[29] K. Leinenweber, M. O'Keeffe, M. Somayazulu, H. Hubert, P. F. McMillan, G. H. Wolf, *Chem. Eur. J.* **1999**, *5*, 3076–3078.
[30] T. D. Boyko, A. Hunt, A. Zerr, A. Moewes, *Phys. Rev. Lett.* **2013**, *111*, 97402-1-97402–5.
[31] S. Bhat, L. Wiehl, S. Haseen, P. Kroll, K. Glazyrin, P. Gollé-Leidreiter, U. Kolb, R. Farla, J. Tseng, E. Ionescu, T. Katsura, R. Riedel, *Chem. Eur. J.* **2020**, *26*, 2187–2194.
[32] C. Braun, Bulk Materials of Doped Multinary Nitrides and Nitridosilicates, Their Production Method and Uses, **2020**, EP20186968.
[33] A. Zerr, G. Miehe, G. Serghiou, M. Schwarz, E. Kroke, R. Riedel, H. Fueß, P. Kroll, R. Boehler, *Nature* **1999**, *400*, 340–342.
[34] M. Schwarz, G. Miehe, A. Zerr, E. Kroke, B. T. Poe, H. Fuess, R. Riedel, *Adv. Mater.* **2000**, *12*, 883–887.
[35] R. Riedel, A. Greiner, G. Miehe, W. Dressler, H. Fuess, J. Bill, F. Aldinger, *Angew. Chem. Int. Ed.* **1997**, *36*, 603–606; *Angew. Chem.* **1997**, *109*, 657–660; *Angew. Chem.* **1997**, *109*, 657–660.
[36] R. Riedel, E. Kroke, A. Greiner, A. O. Gabriel, L. Ruwisch, J. Nicolich, P. Kroll, *Chem. Mater.* **1998**, *10*, 2964–2979.
[37] M. T. Sougrati, A. Darwiche, L. Monconduit, L. Stievano, R. P. Hermann, A. Mahmoud, M. Herlitschke, R. Dronskowski, X. Liu, **2015**, EP15305888.
[38] A. G. Filby, R. A. Howie, W. Moser, *Dalton Trans.* **1978**, *0*, 1797–1799.
[39] K. Dolabdjian, A. L. Görne, R. Dronskowski, M. Ströbele, H.-J. Meyer, *Dalton Trans.* **2018**, *47*, 13378–13383.
[40] C. Braun, Doped Tin Carbodiimide and Use Thereof in Energy Storage Systems and as Phosphors, **2019**, EP19193824.0.
[41] M. Löber, K. Dolabdjian, M. Ströbele, C. P. Romao, H.-J. Meyer, *Inorg. Chem.* **2019**, *58*, 7845–7851.
[42] O. Reckeweg, F. J. DiSalvo, *Z. Anorg. Allg. Chem.* **2003**, *629*, 177–179.
[43] C. Wickleder, *Chem. Mater.* **2005**, *17*, 1228–1233.
[44] C. Wickleder, *J. Alloys Compd.* **2004**, *374*, 10–13.
[45] S. Pagano, G. Montana, C. Wickleder, W. Schnick, *Chem. Eur. J.* **2009**, *15*, 6186–6193.
[46] L. Unverfehrt, M. Ströbele, J. Glaser, H.-J. Meyer, *Z. Anorg. Allg. Chem.* **2009**, *635*, 1947–1952.
[47] J. Sindlinger, J. Glaser, H. Bettentrup, T. Jüstel, H.-J. Meyer, *Z. Anorg. Allg. Chem.* **2007**, *633*, 1686–1690.
[48] J. Hölsä, R.-J. Lamminmäki, M. Lastusaari, P. Porcher, E. Säilynoja, *J. Alloys Compd.* **1998**, *275–277*, 402–406.
[49] S. Yuan, L. Wang, B. Xia, H. Zhang, Y. Yang, G. Chen, *Ceram. Int.* **2017**, *43*, 16018–16022.
[50] S. Yuan, L. Wang, Y. Yang, F. Cheviré, F. Tessier, G. Chen, *Ceram. Int.* **2016**, *42*, 12508–12511.
[51] M. Krings, G. Montana, R. Dronskowski, C. Wickleder, *Chem. Mater.* **2011**, *23*, 1694–1699.
[52] B. Milke, C. Wall, S. Metzke, G. Clavel, M. Fichtner, C. Giordano, *J. Nanopart. Res.* **2014**, *16*, 2795-1-2795–8.
[53] A. Eguía-Barrio, E. Castillo-Martínez, X. Liu, R. Dronskowski, M. Armand, T. Rojo, *J. Mater. Chem. A* **2016**, *4*, 1608–1611.
[54] M. T. Sougrati, J. J. Arayamparambil, X. Liu, M. Mann, A. Slabon, L. Stievano, R. Dronskowski, *Dalton Trans.* **2018**, *47*, 10827–10832.
[55] J. Rodriguez-Carvajal, *Fullprof. 2k-Version 4.40*, **2008**.
[56] T. A. Albright, J. K. Burdett, M.-H. Whangbo, *Orbital Interactions in Chemistry*, 2nd Ed, John Wiley & Sons, **2013**.
[57] J. F. Bérar, P. Lelann, *J. Appl. Crystallogr.* **1991**, *24*, 1–5.
[58] R. H. Herber, *Phys. Rev. B* **1983**, *27*, 4013–4017.
[59] A. Lengyel, Z. Klencsár, Z. Homonnay, P. Sipos, É. G. Bajnóczi, I. Pálinkó, E. Kuzmann, *J. Radioanal. Nucl. Chem.* **2016**, *307*, 1195–1201.
[60] M. Ertl, Z. Ma, T. Thersleff, P. Lyu, S. Huettner, P. Nachtigall, J. Breu, A. Slabon, *Inorg. Chem.* **2019**, *58*, 9655–9662.
[61] C. Liu, F. Xue, H. Huang, X. Yu, C. Xie, M. Shi, G. Cao, Y. Jung, X. Dong, *Electrochim. Acta* **2014**, *129*, 93–99.
[62] Z. Ma, A. Jaworski, J. George, A. Rokicinska, T. Thersleff, T. M. Budnyak, G. Hautier, A. J. Pell, R. Dronskowski, P. Kuśtrowski, A. Slabon, *J. Phys. Chem. C* **2020**, *124*, 152–160.
[63] S. Yuan, Y. Yang, F. Chevire, F. Tessier, X. Zhang, G. Chen, *J. Am. Ceram. Soc.* **2010**, *93*, 3052–3055.
[64] L. Unverfehrt, Neue Verbindungen Der Selten-Erd-Carbodiimide. Synthesen Und Strukturen, Universität Tübingen, **2011**.
[65] R. Y. Babkin, K. V. Lamonova, S. M. Orel, A. M. Prudnikov, Y. G. Pashkevich, O. V. Gornostaeva, O. G. Viagin, P. O. Maksimchuk, Y. V. Malyukin, *J. Lumin.* **2017**, *186*, 247–254.
[66] A. Prudnikov, Y. Pashkevich, K. Lamonova, P. Maksimchuk, O. Viagin, Y. Malyukin, M. Pas'ko , *in Adv. Thin Film. Nanostructured Mater. Coatings* (Ed.: V. Pogrebnjak, Alexander D., Novosad), Springer, Singapore, **2019**, pp. 197–206.
[67] J. J. Arayamparambil, M. Mann, X. Liu, M. Alfredsson, R. Dronskowski, L. Stievano, M. T. Sougrati, *ACS Omega* **2019**, *4*, 4339–4347.

[68] I. A. Courtney, J. R. Dahn, *J. Electrochem. Soc.* **2019**, *144*, 2045–2052.
[69] P. Nash, A. Nash, *Bull. Alloy Phase Diagrams* **1985**, *6*, 350–359.
[70] L. Baggetto, N. A. M. Verhaegh, R. A. H. Niessen, F. Roozeboom, J.-C. Jumas, P. H. L. Notten, *J. Electrochem. Soc.* **2010**, *157*, A340–A347.
[71] G. Kresse, J. Furthmüller, *Comput. Mater. Sci.* **1996**, *6*, 15–50.
[72] G. Kresse, J. Hafner, *Phys. Rev. B* **1994**, *49*, 14251–14269.
[73] G. Kresse, J. Furthmüller, *Phys. Rev. B* **1996**, *54*, 11169–11186.
[74] H. Kim, J.-M. Choi, W. A. Goddard, *J. Phys. Chem. Lett.* **2012**, *3*, 360–363.
[75] C. Adamo, V. Barone, *J. Chem. Phys.* **1999**, *110*, 6158–6170.
[76] P. E. Blöchl, *Phys. Rev. B* **1994**, *50*, 17953–17979.
[77] G. Kresse, D. Joubert, *Phys. Rev. B* **1999**, *59*, 1758–1775.
[78] H. J. Monkhorst, J. D. Pack, *Phys. Rev. B* **1976**, *13*, 5188–5192.
[79] S. N. Steinmann, C. Corminboeuf, *J. Chem. Theory Comput.* **2011**, *7*, 3567–3577.
[80] M. J. Cooper, *IUCr, Acta Crystallogr.* **1964**, *17*, 1452–1456.
[81] J. A. A. Mokuolu, J. C. Speakman, *IUCr, Acta Crystallogr. Sect. B Struct. Crystallogr. Cryst. Chem.* **1975**, *31*, 172–176.
[82] A. L. Beauchamp, D. Goutier, *Can. J. Chem.* **1972**, *50*, 977–981.
[83] I. Agrell, N. Ingri, E. Östlund, G. Bloom, G. Hagen, *Acta Chem. Scand.* **1967**, *21*, 2647–2658.
[84] C. S. Choi, E. Prince, W. L. Garrett, *IUCr, Acta Crystallogr. Sect. B Struct. Crystallogr. Cryst. Chem.* **1977**, *33*, 3536–3537.
[85] U. Müller, *Z. Anorg. Allg. Chem.* **1973**, *399*, 183–192.
[86] A. Schulz, A. Villinger, *Chem. Eur. J.* **2016**, *22*, 2032–2038.
[87] A. D. Becke, K. E. Edgecombe, *J. Chem. Phys.* **1990**, *92*, 5397–5403.
[88] A. Savin, O. Jepsen, J. Flad, O. K. Andersen, H. Preuss, H. G. von Schnering, *Angew. Chem. Int. Ed.* **1992**, *31*, 187–188; *Angew. Chem.* **1992**, *104*, 186–188.
[89] R. Dronskowski, P. E. Bloechl, *J. Phys. Chem.* **1993**, *97*, 8617–8624.
[90] V. L. Deringer, A. L. Tchougréeff, R. Dronskowski, *J. Phys. Chem. A* **2011**, *115*, 5461–5466.
[91] S. Maintz, V. L. Deringer, A. L. Tchougréeff, R. Dronskowski, *J. Comput. Chem.* **2013**, *34*, 2557–2567.
[92] S. Maintz, V. L. Deringer, A. L. Tchougréeff, R. Dronskowski, *J. Comput. Chem.* **2016**, *37*, 1030–1035.
[93] M. Davi, F. Schrader, T. Scholz, Z. Ma, A. Rokicinska, R. Dronskowski, P. Kustrowski, A. Slabon, *ACS Nano* **2018**, *1*, 869–876.
[94] M. Herklotz, J. Weiß, E. Ahrens, M. Yavuz, L. Mereacre, N. Kiziltas-Yavuz, C. Dräger, H. Ehrenberg, J. Eckert, F. Fauth, L. Giebeler, M. Knapp, *IUCr, J. Appl. Crystallogr.* **2016**, *49*, 340–345.
[95] J. P. Perdew, K. Burke, M. Ernzerhof, D.of Physics, N.O.L. 70118 J. Quantum Theory Group Tulane University, *Phys. Rev. Lett.* **1996**, *77*, 3865–3868.
[96] J. P. Perdew, K. Burke, M. Ernzerhof, *Phys. Rev. Lett.* **1997**, *78*, 1396–1396.

Manuscript received: June 3, 2020
Revised manuscript received: August 30, 2020
Accepted manuscript online: September 1, 2020